Title

Targeting Mitochondrial Proline Dehydrogenase with a Suicide Inhibitor to Exploit Synthetic Lethal Interactions with p53 Upregulation and Glutaminase Inhibition

Journal

Molecular Cancer Therapeutics, 18(8)

ISSN

1535-7163

Authors

Scott, Gary K
Yau, Christina
Becker, Beatrice C
et al.

Publication Date

2019-08-01

DOI

10.1158/1535-7163.mct-18-1323

Peer reviewed

HHS Public Access

Author manuscript

Mol Cancer Ther. Author manuscript; available in PMC 2020 February 01.

Published in final edited form as:

Mol Cancer Ther. 2019 August ; 18(8): 1374–1385. doi:10.1158/1535-7163.MCT-18-1323.

Targeting mitochondrial proline dehydrogenase with a suicide inhibitor to exploit synthetic lethal interactions with p53 upregulation and glutaminase inhibition

Gary K. Scott[1], **Christina Yau**[1,2], **Beatrice C. Becker**[1], **Sana Khateeb**[1], **Sophia Mahoney**[1], **Martin Borch Jensen**[1], **Byron Hann**[2], **Bryan J. Cowen**[3], **Scott D. Pegan**[4], **Christopher C. Benz**[1,2]

[1]Buck Institute for Research on Aging, Novato, CA, USA 94945.

[2]Helen Diller Family Comprehensive Cancer Center, University of California, San Francisco, CA, USA 94143.

[3]Department of Chemistry and Biochemistry, University of Denver, Denver, CO, USA 80208.

[4]Center for Drug Discovery, College of Pharmacy, University of Georgia, Athens, GA, USA 30602.

Abstract

Proline dehydrogenase (PRODH) is a p53-inducible inner mitochondrial membrane flavoprotein linked to electron transport for anaplerotic glutamate and ATP production, most critical for cancer cell survival under microenvironmental stress conditions. Proposing that PRODH is a unique mitochondrial cancer target, we structurally model and compare its cancer cell activity and consequences upon exposure to either a reversible (*S*-5-oxo: *S*-5-oxo-2-tetrahydrofurancarboxylic acid) or irreversible (*N*-PPG: *N*-propargylglycine) PRODH inhibitor. Unlike 5-oxo, the suicide inhibitor *N*-PPG induces early and selective decay of PRODH protein without triggering mitochondrial destruction, consistent with *N*-PPG activation of the mitochondrial unfolded protein response (UPR^{mt}). Fly and breast tumor (MCF7)-xenografted mouse studies indicate that *N*-PPG doses sufficient to phenocopy PRODH knockout and induce its decay can be safely and effectively administered *in vivo*. Among breast cancer cell lines and tumor samples, PRODH mRNA expression is subtype-dependent and inversely correlated with glutaminase (GLS1) expression; combining inhibitors of PRODH (*S*-5-oxo, *N*-PPG) and GLS1 (CB-839) produces additive if not synergistic loss of cancer cell (ZR-75–1, MCF7, DU4475, BT474) growth and viability. While PRODH knockdown alone can induce cancer cell apoptosis, the anti-cancer potential of either reversible or irreversible PRODH inhibitors is strongly enhanced when p53 is simultaneously upregulated by an MDM2 antagonist (MI-63, Nutlin-3). However, maximum anti-cancer synergy is observed *in vitro* when the PRODH suicide inhibitor *N*-PPG is combined with both GLS1 inhibition and a p53-upregulating MDM2 antagonist. These findings provide preclinical rationale for the development of *N*-PPG-like PRODH inhibitors as cancer therapeutics to exploit synthetic lethal interactions with p53 upregulation and GLS1 inhibition.

Correspondence to: Christopher C. Benz, Buck Institute for Research on Aging, 8001 Redwood Blvd., Novato, CA 94945; phone: 415-209-2092; fax: 415-899-1802; cbenz@buckinstitute.org.

Conflict of interest disclosure: The authors declare no potential conflicts of interest

Keywords

Proline dehydrogenase (PRODH); p53-inducible; *N*-propargylglycine suicide inhibitor; glutaminase (GLS1) inhibitor; synthetic lethal interactions

Introduction

From prokaryotes to the highest eukaryotes, proline is catabolized by a unique and structurally conserved flavoprotein, proline dehydrogenase (PRODH) (1–3). In eukaryotes PRODH associates with the inner mitochondrial membrane and catalyzes the first and rate limiting catabolic step to yield the intermediate metabolite, pyrroline-5-carboxylate (P5C), with transfer of two electrons to the electron transport chain where they produce either ATP or reactive oxygen species (ROS), as illustrated in Figure 1A. Proline's high metabolic potential of ~30 ATP equivalents/mol is exploited by many insects like flies, whose flight is fueled by proline oxidation and prevented by mutational inactivation of PRODH (4, 5).

PRODH's potential importance in cancer first emerged when it was uncovered by Vogelstein's group as one of the most strongly upregulated genes by the tumor suppressing protein, p53, although its identity was unknown at that time so it was simply referred to as "p53-induced gene 6" (6). PRODH's functional importance in tumor mitochondria grew out of later studies spearheaded by Phang and co-workers stemming from their interest in cancer cell stress responses to nutrient deprivation and hypoxia, as well as the importance of exogenous proline derived from the breakdown of extracellular collagen in sustaining intracellular ATP by anaplerosis (1, 7–10). While the Phang lab's earlier studies indicated that the capacity of PRODH to generate reactive oxygen species (ROS) and induce apoptosis qualified it as a tumor suppressor and provided rationale for its induction by p53 (1, 7), their later studies emphasized the importance of PRODH in sustaining ATP production and cancer cell survival particularly under microenvironmental stress conditions (8–10). Our subsequent studies comparing proline oxidation between insect cells and cancer cell lines suggested that while PRODH can induce mitochondrial ROS production, it likely does so largely via the electron transport chain (e.g. complex I, α-KG dehyrodrogenase complex) from anaplerotic glutamate and α-ketoglutarate production, and not as a direct enzymatic product of inner membrane PRODH activity (11). Today we appreciate that the cancer-specific role of mitochondrial PRODH must be understood within the full proline-P5C cycle, wherein the balance between proline biosynthesis (from glutamate and ornithine via P5C reduction by PYCR1) and proline catabolism (via PRODH) can differentially contribute to cancer cell growth, death, or senescence in various ways (12).

With recognition that a key hallmark of cancer is its reprogramming of normal cell metabolism (13), there has been a resurgence of research into the metabolic pathways commonly altered during oncogenesis along with academic and pharmaceutical discovery efforts to develop small molecule metabolic inhibitors as novel cancer therapeutics (14, 15). In this regard, considerable focus has been given to cancer's rewiring of glutamine metabolism to meet its own cellular energy and biosynthetic needs under microenvironmental stress conditions, most commonly accomplished by activation of the

MYC oncogene which transcriptionally upregulates glutaminase (GLS1) (16). This focus led to the development of a promising and well tolerated new GLS1 inhibitor, CB-839 (Calithera, South San Francisco), now advancing through clinical trials against breast cancer and other human malignancies (17, 18). However, along with such advances came the growing appreciation of the major challenge faced with development of new metabolic inhibitors for cancer therapy, the adaptive ability of cancer cells to utilize alternative metabolic reactions to bypass any well blocked enzyme (15, 16). Thus, it may seem surprising that during development of GLS1 inhibitors, little if any attention was paid to targeting PRODH, arguably an equally important anaplerotic source of mitochondrial glutamate and α-KG production as GLS1, no doubt due in part to the early functional classification of PRODH as a mitochondrial tumor suppressor (1, 7, 9).

Ironically, biochemical searches for PRODH inhibitors predated by at least three decades all efforts to target GLS1 or any other oncogenic metabolic pathways. Instead, these biochemical searches were motivated by the desire to eradicate disease-carrying mosquitoes (4), but were severely limited by lack of purified PRODH enzyme and structural information about the target protein. Not until decades later were the first competitive and irreversible PRODH inhibitors proposed (19), followed by the first derived crystallographic structures of prokaryotic versions of PRODH (2), including one bound to a first-generation competitive inhibitor, L-THFA (20). As a result, it was only very recently that investigators began exploring the use of a PRODH competitive inhibitor like L-THFA as a new cancer therapeutic (21). Concurrently, we independently developed evidence supporting the hypothesis that PRODH represents a unique mitochondrial cancer target and explored structural models of human PRODH to evaluate a potentially more effective irreversible suicide inhibitor. We now describe our chemical biology studies targeting cancer mitochondria with either a second-generation competitive PRODH inhibitor, *S*-5-oxo-2-tetrahydrofurancarboxylic acid (*S*-5-oxo), or with an irreversible suicide inhibitor, *N*-propargylglycine (*N*-PPG), unique in its ability to induce selective mitochondrial decay of PRODH at doses that can be safely administered *in vivo*.

Materials and Methods

Cell lines, antibodies, drugs, and structural models of PRODH-drug interactions

Cell lines were all obtained from American Type Culture Collection (ATCC; Rockville, MD) and immediately frozen (liquid nitrogen) as cell stocks; before each experiment a stock vial was thawed and serially passaged (no more than 10 generations, without further authentication) under 5% CO_2 and 37°C culture conditions as recommended. Routine mycoplasma checks were performed using the MycoAlert detection kit from Lonza (Basel, Switzerland). Antibodies used in this study included the anti-PARP/cPARP (46D11) rabbit monoclonal from Cell Signaling (Danvers, MA); β-actin (C4), PRODH (A-11), NDUFS1 (E-8), and Rieske FeS IgG (A-5) mouse monoclonals from Santa Cruz Biotechnology (Santa Cruz, CA); HRP-conjugated goat anti-mouse secondary from Bio-Rad Laboratories, Inc. (Hercules, CA); α-tubulin mouse monoclonal (T9026) from MilliporeSigma (St. Louis, MO); PRODH and NDUFS1 rabbit polyclonals from ProteinTech™ (Rosemont, IL); Alexa 488 goat anti-mouse and 594 goat anti-rabbit secondaries from Life Technologies (Thermo

Fisher Scientific, Carlsbad, CA); and mouse anti-ATP-synthase α and anti-cytochrome C from BD Biosciences Transduction Labs (San Jose, CA).

CB-839 was provided under MTA from Calithera Biosciences, Inc, (South San Francisco) and MI-63 from Sanofi US (Bridgewater, NJ); nutlin-3 was purchased from Sigma Aldrich/MilliporeSigma, and the *S* and *R* stereoisomers of 5-oxo-2-tetrahydro-furancarboxylic acid (5-oxo) were purchased from MilliporeSigma. DL-propargylglycine (DL-PPG) was purchased from Cayman Chemical Co (Ann Arbor, MI). *N*-propargylglycine (*N*-PPG) was synthesized as follows: 5 g of propargylamine (MilliporeSigma) in 5 mL of DEPC (diethyl pyrocarbonate)-water was slowly mixed over ice with 2 g of iodoacetic acid until fully dissolved. The 10.5 mL reaction mix protected from light was incubated overnight at room temperature and then concentrated (Savant SPD131DDA SpeedVac^{tm} Concentrator, Thermo-Fisher Scientific) down to 4.5 mL, aliquoted into Eppendorf tubes and further dried down to a brown viscous liquid. To separate *N*-PPG from unreacted propargylamine in the pooled mix, 2.5 mL of ethanol was added followed by acetone-ethanol (30.5 mL-3.25 mL) to a final volume of 40 mL, resulting in a light beige *N*-PPG precipitate that was dried, extensively re-washed, and its purity confirmed by HPLC-mass spectrometry and NMR spectroscopy. The newly synthesized compound matched the spectroscopic data for *N*-PPG as previously reported (22) and with >90% purity: ^{1}H-NMR (500 MHz, deuterium oxide) δ 3.94 (d, J = 2.6 Hz, 2H), 3.71 (s, 2H), 2.96 (t, J = 2.6 Hz, 1H).

The three-dimensional (3-D) structure of mammalian PRODH remains experimentally undetermined; however, crystal structures of bacterial PRODH-like catalytic domains bound to either a proline analog or mechanism-based inhibitor have become available over the past decade (20, 23, 24). To estimate at atomic level resolution the 3-D structure of human PRODH bound to either the competitive inhibitor *S*-5-oxo or the suicide inhibitor *N*-PPG we used homology-based structural modelling to align the known primary target sequence of human PRODH with the known 3-D crystal template structure of a prokaryotic PRODH-like catalytic domain (PutA), employing the well validated MODELLER (version 9.19) computational modelling program (25, 26). Specifically, we used the primary amino acid sequence of human PRODH as the target (20–516; GenBank ADD24775.1), the 3-D coordinates of the crystallography resolved 86–610 portion of the *E. coli* PutA dehydrogenase domain complexed to L-THFA (RCSB 1TIW) as the structural template (23), and our homology alignment was based on multiple PutA dehydrogenase sequences including *Bdellovibrio bacteriovorus* (27) and *Sinorhizobium meliloti* (28). The structurally determined position of L-THFA within PutA (1TIW) served as anchor for our homology placement of *S*-5-oxo and *N*-PPG structures within the human PRODH catalytic pocket.

Cell viability and RNA interference (siRNA knockdown) assays

To quantify cell viability, the CellTiter-Glo Cell luminescence-based viability assay (Promega, Madison, WI) was used according to manufacturer's protocol and as previously described (29). Luminescence was measured using a Fluoroskan Ascent FL luminometer (Thermo Scientific, Rockford, IL) to obtain triplicate sample 24, 48 and 72 h time point determinations after treatment, normalized to that of control cells and graphically displayed as mean (+/− SD) percent control values. Coefficient of drug interaction (CDI) values were

determined as previously described by us and others (29, 30), with CDI = %viability(drugA +drugB)/%viability(drugA) × %viability(drugB).

The ON-TARGET plus SMART pool of four different siRNA oligonucleotides to PRODH (J-009543–05-0002, J-009543–06-0002, J-009543–07-0002, and J-009543–08-0002) and a non-specific control siRNA (D-001810–01-05) were all obtained from Dharmacon (GE Dharmacon, Lafayette, CO). Pooled and single oligos were transfected into replicate cell cultures using Lipofectamine 2000 (ThermoFisher Scientific) as we have previously reported (31, 32).

PRODH and GLS1 expression in human breast cancer cell lines and primary breast tumors

Normalized, log2-scaled transcriptome profiles from 51 different breast cancer cell lines, and their corresponding phenotypic assignment into triple negative, HER2+, or Luminal (ER or PR+, HER2-) subtypes, were obtained and analyzed for single gene (PRODH, GLS1) expression levels compared across breast cancer subtypes as previously reported (33, 34). Full genome transcript levels (RNAseq) on 817 primary human breast tumors, originally acquired and analyzed by The Cancer Genome Atlas (TCGA) research network (35, 36), were obtained from their public data deposit site (https://synapse.org), interrogated for PRODH and GLS1 mRNA levels (normalized and log2-scaled transcript per million values), and graphed as box-whisker plots for each of the five different TCGA intrinsic breast cancer subtypes (basal-like, n=136; HER2 enriched, n=65; Luminal-A, n=415; Luminal-B, n=176; Normal-like, 25). Correlations between PRODH and GLS1 expression were tested by Pearson's linear regression (Rp).

Live cell immunofluorescence and laser confocal imaging

ZR-75–1 cells were plated on glass bottom microwell dishes from MatTek Corporation (P35G-1.5–14-C) in RPMI media and incubated with 5 mM *N*-PPG or *S*-5-oxo for 24 hours; 2.5 μL of MitoTracker® Green FM Molecular Probes (Cell Signaling Technology) added to 2 mL of charcoal stripped media (Gibco, Thermo Fisher Scientific, Carlsbad, CA), and 1.5 mL of this mix then added to each well for 30 min after which two drops of NucBlue™ Live Stain Ready Probes™ reagent (Invitrogen by Thermo Fisher Scientific) was added to DAPI counterstain cell nuclei. Immunofluorescent cell imaging was performed as previously described on cells plated and then treated on 4-well glass slides (Lab-Tek®II, MilliporeSigma) using a Zeiss LSM 780 confocal microscope (Zeiss, Dublin, CA) equipped with constant temperature/CO2 regulated enclosure, under 63X oil immersion (31). Plated and treated cells were crosslinked (4% paraformaldehyde) and blocked (10% IGEPAL® CA-630 NP 40 in PBS/DEPC-water with 5% goat serum) and then probed with the indicated primary (overnight) and secondary (90 min) goat anti-mouse or anti-rabbit antibodies and then counterstained with ProLong® Gold antifade reagent with DAPI (Molecular Probes by Life Technologies, Thermo Fisher Scientific) prior to imaging.

Cell and tissue extractions, mitochondrial isolations, and immunoblotting

Snap frozen organs and xenografted tumors were first pulverized under liquid nitrogen and then sonicated in low salt buffer (10 mM Tris pH 7.5, 50 mM NaCl, 0.4% NP40 with protease and phosphatase inhibitors) and extracted as described for cell lines. Cells

harvested at ~70% confluency were washed with ice-cold Dulbecco's phosphate-buffered saline (DPBS) and then harvested in RIPA buffer (50 mM Tris-HCl (pH 8.0), 150 mM NaCl, 1% triton X-100, 0.5% sodium deoxycholate, 0.1% SDS) containing complete Mini, EDTA-free Protease Inhibitor Cocktail tablets (Roche, Indianapolis, IN) and PhosSTOP Phosphatase Inhibitor Cocktail tablets, (Roche); lysates were spun at 14,000 rpm for 5 min and supernatants collected. Intact mitochondria were isolated from the resected and pulverized mouse tissues or freshly harvested ZR-75–1 cells (2 to 4 500 cm^2 dishes at ~90% confluence) as previously described (11); after centrifugation (10,000g × 10 min) the mitochondrial pellets were resuspended in STE (250 mM sucrose, 5 mM Tris-HCl, 2 mM EGTA, pH 7.4) on ice, for either PRODH enzymatic assay or immunoblotting. Prior to immunblotting, protein content was determined by Bradford Coomassie Assay (BCA) kit (Pierce, Rockford, IL) and then diluted into 2X Laemmli sample buffer. Immunoblotting was performed as previously described (29, 31, 32) using polyvinylidene fluoride (PVDF) membranes blocked with 5% non-fat milk in TBST (tris-buffered saline with 0.1% tween-20) incubated with primary and then secondary antibodies conjugated to horse radish peroxidase; the resulting immunoblot signals were scanned for densitometry.

PRODH enzymatic assay

PRODH enzymatic activity was assessed on isolated ZR-75–1 mitochondria by two different bioassays, as we have previously described (11): i) spectrophotometric detection of o-aminobenzaldehyde (oAB) reacting with the proline generated P5C, and ii) time-dependent fluorescence spectrometry monitoring mitochondrial NADH levels as a function of substrate addition and inhibitor treatment. The first assay detects formation of the PRODH specific enzymatic product as P5C-oAB, and the second assay allows for the time-dependent generation of mitochondrial NADH immediately upon addition of proline, pyruvate or malate relative to control (no added substrate) or treatment condition. By comparing proline's NADH generating capacity with that of another substrate such as pyruvate or malate, this more sensitive NADH generating assay enables the indirect bioassay of PRODH specific inhibitors relative to those also affecting other FAD-containing oxidases and comparing the potency or stereospecificity of different enzyme inhibiting candidates. To measure mitochondrial NADH formation, solutions of 40 mM proline and 40 mM malate are first prepared, with or without the inhibitor to be tested, in DEPC-water (GeneMate) with 4 mg/mL rotenone (MilliporeSigma, St Louis, MO) in KHE buffer (120 mM KCl, 3 mM HEPES, 5 mM KH_2PO_4 pH 7.2). Freshly isolated ZR-75–1 mitochondria (0.15 mg resuspended in 30 μL) are mixed with 165 μL of 4 mg/mL rotenone in KHE buffer (to final volume of 195 μL), and the mix aliquoted into a 96-well plate. Into replicate wells 5 μL of 40 mM solution of proline and/or malate is added followed by 5 μL vehicle or enzyme inhibitor, and the time-dependent accumulation of NADH is monitored every 8 sec for up to 30 min on a PHERAStar FS fluorescent microplate reader (BMG LABTECH GmbH, Offenburg, Germany) with $\lambda_{excitation}$ = 340 nm and $\lambda_{emission}$ = 460 nm.

In vivo studies of *N*-PPG treatment and PRODH inhibition in flies and mice

Flies: since their intracellular energy for flight and geotaxis is dependent on high rates of mitochondrial proline catabolism (5, 11), *Drosophila melanogaster* were chosen as a first model to assess the bioavailability and organismal effects of orally administered PPG.

Raised on standard lab food until 7 days of age, male Oregon Red flies (Fly Base, Oregon-R, Roseburg, OR) were then starved for 2 h to synchronize their feeding, transferred to vials (20/vial) containing Whatman paper with 500 μL of 5% w/v sucrose in water +/− 5 mM *N*-PPG (and supplemented daily with 100 μL standard fly food). Fly activity and survival were monitored twice daily; and geotaxis was measured once daily by tapping flies to the bottom of the vial. For comparison with *N*-PPG treated wildtype flies, the same measurements were performed on *slgA* mutant flies lacking functional proline dehydrogenase (5).

Xenografted mice: mouse studies reported here (PTC1797, PTC1854) were all conducted under IACUC approval (AN092211 and AN142193) at the UCSF Cancer Center's Preclinical Therapeutics Core (PTC). MCF7mutER knock-in sublines were chosen for xenografting into 6 week old NCR *nu/nu* athymic female mice (Taconic Farms, Germantown, NY), as these generate subcutaneous MCF7 tumors that grow without the need for supplemental estradiol administration as we have previously described (32). Untreated mice from these earlier studies were used to assess the *in vivo* bioavailability and compare the distant tissue pharmacodynamic effects of intravenous (IV), oral (PO) and intraperitoneal (IP) administration of *N*-PPG. In PTC1797, ten different tumor-implanted mice (#) were given either saline vehicle (#970) or *N*-PPG at 50 mg/kg × 3 (every other day) by either PO gavage (#965, #966, #967), IV (#962, #925, #968) or IP (#963, #964, #969) treatments. In PTC1854, three different mice were treated with nine daily PO doses of either saline (#3883) or 50 mg/kg *N*-PPG (#3840, #3880), begun 58 days after tumor implantation. The tolerance of these mice to either vehicle or *N*-PPG treatments was assessed by daily monitoring of animal health and activity and twice weekly measurement of animal body weight. In both of these mouse studies no animal lost ≥ 10% of body weight, and the overall health and activity of all *N*-PPG treated mice appeared identical to that of controls. In PTC1854, tumor growth was measured by calipers along the largest (length) and smallest (width) axes, and tumor volumes were calculated by the following formula: tumor volume = [(length) × (width) × (width)] / 2. At the conclusion of each mouse study all animals were euthanized, kidneys (in PTC1797) and tumors (in PTC1854) were resected and snap frozen into liquid nitrogen within 2 h of the final *N*-PPG treatment for subsequent mitochondrial extraction or whole tissue protein extraction.

Statistics

Technical and biological replicates were performed as described in figure legends, and data analyzed by GraphPad Prism 7 (La Jolla, CA) or Bioconductor R (www.bioconductor.org) software programs. Graphical plots show single, median or mean (+/− SD) values. All replicate measures were statistically compared by ANOVA F-test (e.g. box-whisker plots) or 2-tailed Student's t test; and correlations were determined by Pearson's linear regression (Rp). Significant differences were determined as *P <0.05 or **P <0.01.

Results

Assaying and modelling human PRODH inactivated by either a competitive proline analog or an irreversible mechanism-based inhibitor

While cancer cells catabolize proline to produce anaplerotic carbon for energy (ATP) production and biosynthesis, the immediate product of proline catabolism by PRODH is the imino acid, pyrroline-5-carboxylate (P5C), in rapid equilibrium with glutamate semi-aldehyde that is further oxidized by P5C dehydrogenase (P5CDH) to glutamate (Figure 1A). As we have previously shown (11), mitochondrial P5C production can be directly detected as a colored adduct when reacted with o-aminobenzaldehyde (oAB), forming P5C-oAB (Suppl. Figure 1A); however, as we have also shown (11) a more sensitive albeit indirect measure of mitochondrial PRODH activity is to monitor the time-dependent accumulation of NADH upon mitochondrial exposure to proline in the presence of rotenone to prevent complex 1 reoxidation of NADH (Figure 1A, B). By substituting for the substrate proline this assay can detect and compare the oxidative formation of NADH by different mitochondrial enzymes (Suppl. Figure 1B); and by adding proline and either pyruvate or malate sequentially after pre-exposure to a PRODH-specific inhibitor, this assay can be used to either compare active (L-THFA, 5-oxo) vs. inactive (furoic, furan) structural analogs as competitive inhibitors or to test their stereospecificity (5 mM *S*-5-oxo of *R*-5-oxo) as competitive inhibitors (Suppl. Figure 1C). By comparing equimolar exposures to different inhibitors, we used this assay to show that *R*-5-oxo is inactive, that *S*-5-oxo is significantly more active than L-THFA, that the mechanism-based PRODH inhibitor *N*-PPG appears to be more potent than the competitive PRODH inhibitor *S*-5-oxo (Suppl. Figure 1D), and that a series of propargyl structural analogs, including the isomer DL-PPG, cannot significantly inhibit PRODH enzymatic activity (Suppl. Figure 2). Furthermore, when a 30 min mitochondrial washout step was inserted between inhibitor pre-treatment and sequential substrate additions, washout completely eliminated the PRODH inhibitory effect of 5 mM *S*-5-oxo while retaining the inhibitory effect of *N*-PPG, demonstrating the specific and irreversible inhibition of PRODH by *N*-PPG in the absence of any other inhibitory effect on mitochondrial NADH production by either malate or pyruvate oxidation (Figure 1B, Suppl. Figure 1B).

To better understand the chemical and biological basis underlying and differentiating PRODH inhibition by either *S*-5-oxo or *N*-PPG, and given that there is as yet no experimentally determined three dimensional (3-D) atomic level structure for mammalian PRODH, we employed a well validated homology-based computational modelling program, MODELLER (25, 26), to produce a 3-D structure of human PRODH bound to these inhibitors by aligning the known primary amino acid sequence of human PRODH with the experimentally determined 3-D structural coordinates of the PutA dehydrogenase domain from *E coli* (23). From our *S*-5-oxo bound PRODH model (Figure 1C), we observed its probable hydrogen bond formation with tyrosine (Y548) and arginine (R564, R563) to stabilize this competitive inhibitor within the PRODH catalytic pocket. In contrast, we compared the expected pre-reactive configuration of *N*-PPG within PRODH with its presumed pocket stabilized covalent adduction to the N(5) of FAD (Figure 1D). This post-reactive *N*-PPG-PRODH structure is likely similar to the reported crystal structure of *E. coli*

PutA irreversibly inactivated by *N*-PPG that showed bicovalent linkage of *N*-PPG with PutA FAD N(5) and the ε-amino of a PutA pocket lysine, K329 (37). This specific active site K residue is evolutionarily conserved and corresponds to K234 in human PRODH (Figure 1D). Assuming a conserved mechanism of inactivation, we predict that the reaction of human PRODH with *N*-PPG results in a 2-carbon covalent link between the epsilon nitrogen of K234 and the N5 atom of the reduced FAD (Figure 1D). Because the covalently modified FAD is irreversibly locked into a reduced electronic state, the enzyme is unable to redox cycle and is therefore inactive. Notably, this type of bicovalent pocket reaction differs from a similar FAD facilitated inhibition of human mitochondrial monoamine oxidase (MAO)-B where the PPG-like *N*-propagyl-1(*R*)-aminoindan (Rasagiline) is covalently bound to FAD N(5) but not also to a pocket residue (38). Of likely functional significance, inactivation of human PRODH by *N*-PPG is predicted to cause major distortion of the active site, including butterfly bending of the FAD isoalloxazine, crankshaft rotation of the FAD ribityl chain into the reduced conformation, and movement of the α8 helix into an open conformation. All of these structural distortions are incompatible with binding by the substrate proline.

The suicide inhibitor N-PPG induces selective decay of PRODH protein without triggering mitochondrial destruction, consistent with activation of the mitochondrial unfolded protein response (UPR^{mt})

Confocal imaging of PRODH expression in ZR-75–1 cells treated over 72 h with either vehicle, *S*-5-oxo or *N*-PPG (5 mM) showed the exclusive mitochondrial localization of PRODH as expected but revealed early (within 24 h) decay of PRODH protein only upon *N*-PPG exposure (Figure 2A). This microscopic observation was confirmed by western blotting which also showed that the *N*-PPG isomer, DL-PPG, does not induce PRODH decay (Figure 2B), and further demonstrated the progressive and selective 24–72 h loss of PRODH protein (normalized to β-actin and untreated control ratio) in the absence of any concurrent decline in either mitochondrial NADH-ubiquinone oxidoreductase NDUFS1 or cytosolic methylenetetrahydrofolate reductase MTHFR flavoprotein (Figure 2C). The mitochondrial chaperonin, Heat Shock Protein 60 (HSP60), is responsible for folding more than 300 mitochondrial matrix proteins and physically interacting with the mitochondrial protease LONP to maintain mitochondrial proteostasis as a proposed mediator of the mitochondrial unfolded protein response (UPR^{mt}) (39–42). As such, we observed an induction of total cell and mitochondrial-localized HSP60 coincident with the initiation of PRODH decay during the first 24 h of *N*-PPG exposure, that was not apparent following *S*-5-oxo exposure (Figure 2D). While the preservation of NDUFS1 expression largely ruled out *N*-PPG induced mitophagy (43), we employed confocal imaging to revisit the question of mitophagy vs. UPR^{mt} induction by visually assessing mitochondrial membrane integrity and looking for membrane recruitment of the PINK1/PARKIN complex (known to recruit the mitophagic machinery) relative to mitochondrial import of the GRP-75 chaperone (known to be associated with UPR^{mt}) during the initial period (24 h) of *N*-PPG induced PRODH decay. In keeping with our western blot data as described, confocal images of control and *N*-PPG treated ZR-75–1 cell cultures showed early loss of mitochondrial PRODH expression without loss of mitochondrial membrane structure as assessed by the outer membrane protein TOM20 (Figures 3A, 3B), no evident membrane recruitment of PINK1/PARKIN complex despite mitochondrial import of GRP-75 (Suppl. Figure 3) and no decline in the

extramitochondrial FAD-containing enzyme MTHFR (Figures 3C, 3D). The right top and bottom panels (Figure 3C, 3D) show a similar but independent experiment as that shown in the left panels (Figure 3A, 3B), except that control and *N*-PPG treated ZR-75–1 cells were stained for PRODH using different primary and fluorochrome-conjugated secondary antibodies to control for potential differences in primary immunoreactivity and non-specific secondary antibody effects. Merged imaging confirmed the different subcellular localizations of PRODH and MTHFR as well as the colocalization of mitochondrial PRODH and TOM20

Fly and mouse studies indicate that systemically bioavailable N-PPG at doses sufficient to induce PRODH decay can be safely administered in vivo

Since *SlgA* null mutant flies that lack systemic PRODH activity are known to be viable, fertile and with normal lifespan, yet possess a characteristic and easily recognizable *Sluggish-A* phenotype (5), we fed fruit flies millimolar concentrations of *N*-PPG in sucrose for several days to assess its oral bioavailability and systemic activity. Within 48 h the orally fed *N*-PPG (5 mM) treated flies exhibited clear loss of geotaxis relative to control fed flies (Supplementary Video S1A) perfectly phenocopying the *Sluggish-A* phenotype (Supplementary Video S1B) without any loss in fly vitality, indicating its efficient oral bioavailability and systemic biological activity. Based on these fly results, studies of *N*-PPG bioavailability and tolerance were then undertaken in nude mice implanted with MCF7mutER xenografts capable of tumorigenic growth in the absence of exogenous estradiol supplementation (32). Untreated xenografted mice from two recently reported studies (PTC1797, PTC1854) were used to assess the *in vivo* bioavailability and distant tissue pharmacodynamic effects of either IV, PO or IP administered *N*-PPG at a dose (50 mg/kg) estimated to achieve up to 5 mM systemic blood concentrations (although direct assays of *N*-PPG were not available). In PTC1797, ten different control and *N*-PPG treated mice (#) were given either vehicle alone (#970) or *N*-PPG at 50mg/kg × 3 (every other day) by either PO gavage (#965, #966, #967), IV (#962, #925, #968) or IP (#963, #964, #969) administration. In a follow-up study, PTC1854, three different mice were treated with nine daily PO doses of either saline (#3883) or 50 mg/kg *N*-PPG (#3840, #3880), begun 58 days after tumor implantation. In both these murine studies no mouse lost ≥ 10% of body weight, and the overall health and activity of all *N*-PPG treated mice appeared identical to that of vehicle treated controls. Based on Genotype-Tissue Expression (https://commonfund.nih.gov/gtex) and Human Protein Atlas (https://www.proteinatlas.org/cell) databases indicating that human kidneys (especially tubule cells) express high PRODH mRNA and protein levels relative to many other normal organs, mouse kidneys were excised and evaluated at the conclusion of PTC1797 to look for biological evidence of *N*-PPG induced PRODH decay. The total number of study mice was insufficient to statistically compare *N*-PPG effects based on different routes of administration; however, Figure 4A demonstrates that following three (every other day) doses of *N*-PPG relative to vehicle treatment, the various routes of *N*-PPG administration (IV, PO, IP) were each able to affect at least 60% reduction in mouse kidney PRODH protein levels (normalized to ATP synthase). In the more limited PTC1854 study, *N*-PPG given orally over nine days was evaluated for its potential tumor bioavailability and pharmacodynamic impact. As shown in Figure 4B, despite the xenografted tumors' lack of normal vasculature and the relative

resistance of the parental MCF7 breast cancer line's *in vitro* growth to continuous millimolar exposure of *N*-PPG, the *in vivo* treated xenografts showed modest evidence of *N*-PPG induced decay in tumor cell mitochondrial PRODH expression (~20–50% reduction, normalized to ATP synthase) with slight impact on the tumors' volumetric growth during that treatment period (Figure 4C).

PRODH loss of function is synthetically lethal in combination with GLS1 loss of function and p53 upregulation

Since PRODH provides a bypass carbon source for glutamate-addicted and GLS1 overexpressing cancers (16), particularly those proving sensitive to clinically emergent GLS1 inhibitors like CB-839 (17, 18), we investigated the cancer cell relationship between PRODH and GLS1 expression using publically available transcriptome data from 51 different human breast cancer cell lines (34) and 817 primary breast tumors molecularly characterized and classified by the TCGA according to their intrinsic subtypes (36). In both the cell line and primary tumor transcriptome datasets, PRODH mRNA expression varied significantly by intrinsic breast cancer subtype, with luminal and HER2+ tumors showing the highest and basal/triple-negative tumors showing the lowest levels of PRODH mRNA expression (Figure 5A, 5B). Irrespective of breast cancer subtype, PRODH and GLS1 mRNA levels showed significant inverse correlations most pronounced among the cell lines ($Rp = -0.52$; $p = 9.02E\text{-}5$) but also apparent among the primary breast tumors ($Rp = -0.12$; $p = 0.0006$), and consistent with the idea that one or the other of these GLS1 and PRODH pathways are needed to feed breast cancer's anaplerotic addiction to glutamate (16). Comparing PRODH inhibitors *S*-5-oxo and *N*-PPG for their ability to at least additively enhance the antitumor activity of the GLS1 inhibitor CB-839, we demonstrated this to be true against MCF7 breast cancer cells in culture (Figure 5C) but not against the non-malignant breast epithelial cell line, MCF10A, whose growth in culture remained unaffected by PRODH and/or GLS1 inhibition (Figure 5D).

The variable expression of PRODH among human breast and other cancers is primarily due to its positive transcriptional control by the tumor suppressing protein p53 (1, 6), as well as some negative control by MYC upregulation (44), consistent with the fact that most basal/triple-negative (and MYC upregulated) breast cancers possess mutationally inactivated p53, while most luminal (ER/PR+) and HER2+ breast cancers express wildtype and functionally active p53 protein (Figure 5A, left panel). The luminal breast cancer lines MCF7, DU4474 and ZR-75–1, as well as the non-malignant breast epithelial cells MCF10A, express varying basal levels of p53 and PRODH, and both of these proteins are variably upregulated within 24 h of exposure to an MDM2 antagonist like nutlin-3 or MI-63 (Figure 6A). As we and others have previously shown (45, 46), the post-translational induction of p53 by such MDM2 antagonists produces either cancer cell senescence or apoptosis, the latter marked by an increase in PUMA and cleaved (c) PARP protein evident only in p53 wildtype expressing cancer cells but not in more minimally PRODH expressing non-malignant cells like MCF10A cells (Figure 6A). Following siRNA knock-down of PRODH in luminal breast cancer cell lines, cPARP is induced and this apoptosis indicator is further enhanced by 24–48 h pretreatment of siRNA treated cells with a p53-upregulating MDM2 antagonist (Figure 6B). Since both GLS1 inhibition and MDM2 antagonism each produced anticancer effects

that were at least additive in combination with PRODH loss of function, we compared these treatments when given to DU-4475 or ZR-75–1 cells in combination with either the competitive (*S*-5-oxo) or suicide (*N*-PPG) PRODH inhibitors. As seen in Figure 6C and numerically demonstrated by calculating a coefficient of drug interaction (CDI) for each 2- and 3-drug combination, significant synergy (CDI <0.70; $p < 0.05$) was observed in both cancer cell lines and for nearly all 2-drug (PRODH inhibitor + MDM2 antagonist or GLS1 inhibitor) and 3-drug (PRODH inhibitor + MDM2 antagonist + GLS1 inhibitor) combinations, as might be expected for "synthetically lethal" interactions between these pathway-targeted therapeutics. When comparing the two types of PRODH inhibitors, the 2- and 3-drug combinations that included *N*-PPG nearly always appeared more cytotoxic than those involving *S*-5-oxo; however, since these differences did not reach statistical significance, more extensive *in vitro* and *in vivo* comparisons are needed to confirm if *N*-PPG is indeed a more effective anticancer agent than *S*-5-oxo.

Discussion

The quest for PRODH inhibitors goes back more than 40 years when this was considered a possible approach to eradicate tsetse flies and prevent African trypanosomiasis (4). While the first mechanism-based PRODH inhibitor was proposed in 1993 (19), further progress in this effort was stymied until a decade later when Tanner's group generated the first crystal structure of a prokaryotic bifunctional precursor of PRODH known as PutA (2). The following year, Tanner's group reported the first crystal structure of a bacterial PRODH complexed with the competitive inhibitor L-THFA (23). Subsequent crystal structures of other bacterial PRODHs showed that the binding mode of L-THFA is highly conserved (20, 28). Together, these structural studies employing prokaryotic forms of PRODH provided the foundation for our computer modeling of human PRODH bound to either the *S*-stereoisomer of 5-oxo, newly identified in this study as a second-generation competitive PRODH inhibitor more potent than L-THFA, or to the irreversible suicide inhibitor, *N*-PPG. Tanner's group showed that *N*-PPG is a mechanism-based covalent inactivator of four different bacterial PRODHs, which have pairwise sequence identity as low as 27% (24, 27, 37). In each case, the structure of the inactivated enzyme shows a covalent link between the FAD N5 atom and a conserved active site lysine (K) residue. Homology modeling strongly suggests that human and bacterial PRODHs share a conserved active site structure, including the K residue implicated in the *N*-PPG inactivation mechanism ((12) and Figures 1C, 1D).

With more recent elucidation of additional PRODH structures recognizing its evolutionarily conserved higher order $(\beta\alpha)_8$-barrel structure (27, 28) predicted to form within residues 121–579 of human PRODH, along with the use of protein structure modelling algorithms it now appears that the bicovalent *N*-PPG inhibitory mechanism known to occur in bacterial PutAs may similarly occur in human PRODH. Unlike other propargylic (PPG-like) analogs like Rasagiline, an FDA-approved selective and irreversible inhibitor of the FAD-containing monoamine oxidase (MAO)-B currently used to treat Parkinson's disease (38), our model predicts that *N*-PPG bicovalently binds and irreversibly inhibits human PRODH by tethering FAD to a pocket K residue. Using our MODELLER generated human PRODH structure, K234 appears to be the most likely candidate for pocket adduction by *N*-PPG, in agreement with a recent SWISS-MODEL homology solution showing proximity of this K234 residue

to a pocket bound L-THFA (12). However, our model also suggests that another lysine at position K326, which is part of a conserved KLS motif similar to that found in *E. coli* PutA, however unlikely based on bacterial studies could become an alternative candidate for involvement in *N*-PPG-PRODH adduct formation, pointing to the critical need for an experimentally determined 3-D structure of human PRODH following renewed efforts to overcome the current challenges limiting bacterial production of recombinant human PRODH (47). In conjunction with our model suggesting that *N*-PPG covalently binds and distorts the human PRODH catalytic pocket, we also demonstrate that its activity as a suicide inhibitor in living cells is associated with induction of intramitochondrial PRODH protein decay, likely mediated by a UPR^{mt} mechanism and not similarly activated by a competitive PRODH inhibitor like *S*-5-oxo or by the *N*-PPG isomer, DL-PPG, which also fails to inhibit PRODH activity.

Mass spectrometry and NMR confirmed the ≥ 90% purity of our newly synthesized *N*-PPG, but given the ubiquity of flavoproteins like PRODH our earliest concern focused on the specificity of *N*-PPG as a PRODH inhibitor. This concern was largely mitigated by prior knowledge that FAD association with the TIM barrel structure of PRODH occurs in only one other known instance (23), rendering PRODH's catalytic site a relatively unique molecular target not readily susceptible to other PPG-like structural analogs. Nonetheless, rather than assaying the inhibitory effect of *N*-PPG on PRODH by simply measuring mitochondrial P5C generation (the first product of proline catabolism by PRODH), we chose to monitor the time-dependent generation of mitochondrial NADH by oxidation of individually introduced substrates including proline, malate and pyruvate, enabling us to show that *N*-PPG inhibits PRODH specifically and irreversibly, without affecting other mitochondrial NADH generating enzymes. Following our initial and surprising observation that *N*-PPG, but not *S*-5-oxo or DL-PPG, treatment of cultured cancer cells produces an early (within 24 h) decline in PRODH protein levels, we employed both confocal microscopy and western blotting to confirm the specificity of this protein degrading effect on PRODH not seen in other mitochondrial or extramitochondrial FAD-containing enzymes, and occuring without loss of total cell mitochondria, their outer membrane constituent TOM20 or its recruitment of PINK1, thereby excluding PPG induced mitophagy (43).

Understanding that UPR^{mt} is often experimentally activated by introducing a structural distortion in a single intramitochondrial protein (41), and given our model's suggestion that bicovalent adduction of PPG to FAD and a nearby residue like K234 produces structural distortion of the PRODH catalytic pocket, we probed for and observed *N*-PPG-specific induction of two mitochondrial chaperone proteins, HSP60 and GRP-75, coincident with PRODH decay and consistent with mechanistic induction of UPR^{mt} (40–42). Of interest, targeting mitochondrial HSP60 has very recently been shown to be a promising new anticancer strategy with little if any toxic impact on normal cells (42), suggesting that the combination of PRODH-targeted *N*-PPG therapy with an HSP60-targeted agent is worth exploring.

Although an orally bioavailable propargylic analog that inhibits and covalently reacts with its FAD-containing enzymatic target has been successfully developed and approved for medical use (38), the *in vivo* administration of *N*-PPG has never been reported. In fact, only

very recently has the first *in vivo* administration of a PRODH competitive inhibitor, L-THFA, been reported (21). Giving daily intraperitoneal (IP) injections of up to 60 mg/kg of L-THFA into mice bearing small orthotopic implants of murine breast cancer cells, these investigators observed excellent host tolerance to this competitive PRODH inhibitor and, after 16–18 days of sequential treatment, showed that it can reduce pulmonary metastasis formation by 50% without any significant impact on primary tumor growth (21). We explored *in vivo* administration of *N*-PPG first in flies, where oral consumption of 5 mM *N*-PPG (in sucrose) led to loss of geotaxis within 48 h, phenocopying the *SlgA* mutant fly strain lacking all PRODH activity; and this *N*-PPG induced loss of *Drosophila* flight muscular energy occurred without detectable loss in fly vitality or fertility. Using nude mice xenografted with engineered human breast cancer cells capable of estrogen-independent *in vivo* tumor growth, whose parental cell line (MCF7) is only modestly growth inhibited *in vitro* by 5 mM *N*-PPG, we observed excellent host tolerance to repeated 50 mg/kg administration of *N*-PPG given by either oral, intraperitoneal or intravenous routes of administration. Although not powered to statistically compare *N*-PPG systemic bioavailability between these different routes of administration or to comprehensively assess *N*-PPG effects on xenografted tumor growth, these mouse studies clearly demonstrated that *N*-PPG at this dose and schedule via all routes of administration could reduce PRODH protein levels in both normal tissue (kidneys) and xenografted tumors. The ability to read out a systemic pharmacodynamic effect from *N*-PPG as tissue/cell loss of mitochondrial PRODH protein expression, apart from signifying a functionally different cellular consequence induced by this mechanistically unique inhibitor, offers a novel future advantage in monitoring tissue exposure to this suicide PRODH inhibitor, unlike the more complex metabolomic measures required to monitor tissue or tumor responses to a competitive PRODH inhibitor like L-THFA (21). Given that both normal and tumor tissues react similarly to *N*-PPG with degradation of mitochondrial PRODH protein, likely occuring by a common UPR^{mt} mechanism, and appreciating that inhibition of PRODH function is deleterious to malignant but not normal mammalian cells (21), it is noteworthy that UPR^{mt} induction is now considered a promising new cancer treatment strategy in itself (39) that is not only nontoxic to normal cells but, in fact, increasingly recognized as beneficial to normal growth and development by enhancing cell vitality and potentially increasing organismal longevity (41).

As with other anticancer strategies, inhibiting PRODH is not to be envisioned as a monotherapy, especially given that metabolic reprograming as a hallmark of cancer is highly adaptive and subject to, as well as capable of inducing, epigenetic shifts in cancer cell phenotypes associated with altered responsiveness to a wide variety of anticancer agents (13–15). One proven approach to identifying more effective anticancer strategies now being considered in the context of oncometabolic targets is the identification of synthetic lethality-based treatment combinations (15). In this study we demonstrate strong biological inter-relationships underlying cancer cell mitochondrial addiction to glutamate, manifest as either PRODH or GLS1 dependence, and between PRODH transcriptional stimulation and MDM2 antagonists that upregulate p53wt. Common to the preclinical studies of all three of these emerging cancer targets (MDM2, GLS1, PRODH) is that their individual inhibition in normal or non-malignant host tissues is not cytotoxic and is commonly well tolerated (16,

21, 46), although their combinatorial tolerance *in vivo* remains to be assessed. We now provide experimental rationale compelling future *in vivo* evaluation of synthetic lethality-based 2- and 3-drug combinations involving a PRODH inhibitor (e.g. *S*-5-oxo or *N*-PPG), a GLS1 inhibitor (e.g. CB-839), and a p53-upregulating MDM2 antagonist (e.g. MI-63 or nutlin-3). In particular, based on our chemical biology modelling and because of its novel pharmacodynamic advantage in terms of inducing measurable reductions in distant tissue/tumor mitochondrial PRODH expression, the suicide inhibitor *N*-PPG may now be considered the preferred drug of choice in pursuing future *in vivo* studies focusing on the anticancer utility of PRODH inhibition. Therefore, given its pharmacodynamic advantage as well as its seemingly greater potency over competitive inhibitors like L-THFA or *S*-5-oxo, the suicide inhibitor *N*-PPG should be advanced further into preclinical studies designed to exploit and evaluate its potential synthetic lethal interactions with p53 upregulation and inhibition of GLS1.

Supplementary Material

Refer to Web version on PubMed Central for supplementary material.

Acknowledgments

We appreciate the many technical contributions from Buck Institute scientists Katya Frazer, Daniel Rothschild, and Mauricio Ortega. In addition, we wish to sincerely thank one of the anonymous expert reviewers of this manuscript for specific suggestions that substantially enhanced the accuracy and presentation of our study results.

Financial support: Elizabeth MA Stevens memorial funding (C. C. Benz); Alfred Benzon Fellowship & NIA-1K99AG056680 (M. B. Jensen).

References

1. Donald SP, Sun XY, Hu CA, Yu J, Mei JM, Valle D, Phang JM. Proline oxidase, encoded by p53-induced gene-6, catalyzes the generation of proline-dependent reactive oxygen species. Cancer Res 2001; 61:1810–1815. [PubMed: 11280728]
2. Lee YH, Nadaraia S, Gu D, Becker DF, Tanner JJ. Structure of the proline dehydrogenase domain of the multifunctional PutA flavoprotein. Nat Struct Biol 2003; 10:109–114. [PubMed: 12514740]
3. Servet C, Ghelis T, Richard L, Zilberstein A, Savoure A. Proline dehydrogenase: a key enzyme in controlling cellular homeostasis. Frontiers in Bioscience 2012; 17: 607–620.
4. Hargrove JW. Amino acid metabolism during flight in tsetse flies. J Insect Physiol 1976; 22:309–313. [PubMed: 1249439]
5. Hayward DC, Delaney SJ, Campbell HD, Ghysen A, Benzer S, Kasprzak AB, Cotsell JN, Young IG, Miklos GL. The sluggish-A gene of Drosophila melanogaster is expressed in the nervous system and encodes proline oxidase, a mitochondrial enzyme involved in glutamate biosynthesis. Proc Natl Acad Sci USA 1993; 90: 2979–2983. [PubMed: 8096642]
6. Polyak K, Xia Y, Zweier JL, Kinzler KW, Vogelstein B. A model for p53-induced apoptosis. Nature 1997; 389:300–305. [PubMed: 9305847]
7. Pandhare J, Cooper SK, Donald SP, Phang JM. Regulation and function of proline oxidase under nutrient stress. J Cell Biochem 2009; 107: 759–768. [PubMed: 19415679]
8. Liu W, Glunde K, Bhujwalla ZM, Raman V, Sharma A, Phang JM. Proline oxidase promotes tumor cell survival in hypoxic tumor microenvironments. Cancer Res 2012; 72: 3677–3686. [PubMed: 22609800]
9. Liu W, Phang JM. Proline dehydrogenase (oxidase), a mitochondrial tumor suppressor, and autophagy under the hypoxia microenvironment. Autophagy 2012; 8: 1407–1409. [PubMed: 22885468]

10. Phang JM, Liu W, Hancock C, Christian KJ. The proline regulatory axis and cancer. Front Oncol 2012; 2: 60. [PubMed: 22737668]
11. Goncalves RLS, Rothschild DE, Quinlan CL, Scott GK, Benz CC, Brand MD. Sources of superoxide/H2O2 during mitochondrial proline oxidation. Redox Biology 2014; 2: 901–909. [PubMed: 25184115]
12. Tanner JJ, Fendt S-M, Becker DF. The proline cycle as a potential cancer therapy target. Biochemistry 2018; 57: 3433–3444. [PubMed: 29648801]
13. Hanahan D, Weinberg RA. Hallmarks of cancer: the next generation. Cell 2011; 144: 646–674. [PubMed: 21376230]
14. Martinez-Outschoorn UE, Peiris-Pages M, Pestell RG, Sotgia F, Lisanti MP. Cancer metabolism: a therapeutic perspective. Nat Rev Clin Oncol 2017; 14: 11–31. [PubMed: 27141887]
15. Bajpai R, Shanmugam M. Targeting cancer metabolism through synthetic lethality-based combinatorial treatment strategies. Curr Opin Oncol 2018; 30: 338–344. [PubMed: 29994904]
16. Atman BJ, Stine ZE, Dang CV. From Krebs to clinic: glutamine metabolism to cancer therapy. Nat Rev Cancer 2016; 16: 619–634. [PubMed: 27492215]
17. Katt WP, Cerione RA. Glutaminase regulation in cancer cells: a druggable chain of events. Drug Discov Today 2014; 19: 450–457. [PubMed: 24140288]
18. Gross MI, Demo SD, Dennison JB, Chen L, Chernov-Rogan T, Goyal B, Janes JR, Laidig GJ, Lewis ER, Li J, MacKinnon AL, Parlati F, Rodriguez MLM, Shwonek PJ, Sjogren EB, Stanton TF, Wang T, Yang J, Zhao F, Bennett MK. Antitumor activity of the glutaminase inhibitor CB-839 in triple-negative breast cancer. Mol Cancer Ther 2014; 13: 890–901. [PubMed: 24523301]
19. Tritsch D, Mawlawi H, Biellmann JF. Mechanism-based inhibition of proline dehydrogenase by proline analogues. Biochim Biophys Acta 1993; 1202: 77–81. [PubMed: 8373828]
20. Luo M, Arentson BW, Srivastava D, Becker DF, Tanner JJ. Crystal structures and kinetics of monofunctional proline dehydrogenase provide insight into substrate recognition and conformational changes associated with flavin reduction and product release. Biochemistry 2012; 51: 10099–10108. [PubMed: 23151026]
21. Elia I, Broekaert D, Christen S, Boon R, Radaelli E, Orth MF, Verfaillie C, Grunewald TGP, Fendt S-M. Proline metabolism supports metastasis formation and could be inhibited to selectively target metastasizing cancer cells. Nature Communications 2017; 8: 15267.
22. Struthers H, Springler B, Mindt TL, Schibli R. “Click-to-chelate”: design and incorporation of triazole-containing metal-chelating systems into biomolecules of diagnostic and therapeutic interest. Chem Eur J 2008; 14: 6173–6183. [PubMed: 18494020]
23. Zhang M, White TA, Schuermann JP, Baban BA, Becker DF, Tanner JJ, Structures of the Escherichia coli PutA proline dehydrogenase domain in complex with competitive inhibitors. Biochemistry 2004; 43: 12539–12548. [PubMed: 15449943]
24. White TA, Joshnson WH Jr, Whitman CP, Tanner JJ. Structural basis for the inactivation of Thermus thermophilus proline dehydrogenase by N-propargylglycine. Biochemistry 2008; 47: 5573–5580. [PubMed: 18426222]
25. Webb B, Sali A. Comparative Protein Structure Modeling Using MODELLER. Curr Protoc Bioinformatics 2016; 54: 54:5.6.1–5.6.37.
26. Webb B, Sali A. Protein structure modeling with MODELLER. Methods Mol Biol 2017; 1654: 39–54. [PubMed: 28986782]
27. Korasick DA, Singh H, Pemberton TA, Luo M, Dhatwalia R, Tanner JJ. Biophysical investigation of type A PutAs reveals a conserved core oligomeric structure. FEBS J 2017; 284: 3029–3049. [PubMed: 28710792]
28. Luo M, Gamage TT, Arentson BW, Schlasner KN, Becker DF, Tanner JJ. Structures of proline utilization A (PutA) reveal the fold and functions of the aldehyde dehydrogenase superfamily domain of unknown function. J Biol Chem 2016; 291; 24065–24075. [PubMed: 27679491]
29. Wison-Edell KA, Yevtushenko MA, Rothschild DE, Rogers AN, Benz CC. mTORC1/C2 and pan-HDAC inhibitors synergistically impair breast cancer growth by convergent AKT and polysome inhibiting mechanisms. Breast Cancer Res Treat 2014; 144: 287–298. [PubMed: 24562770]

30. Li X, Lin Z, Zhang B, Guo L, Liu S, Li H,Zhang J, Ye Q. β-elemene sensitizes hepatocellular carcinoma cells to oxaliplatin by preventing oxaliplatin-induced degradation of copper transporter 1. Sci Rep 2016; 6: 21010. [PubMed: 26867799]

31. Marx C, Held JM, Gibson BW, Benz CC. ErbB2 trafficking and degradation associated with K48 and K63 polyubiquitination. Cancer Res 2010; 70: 3709–3717. [PubMed: 20406983]

32. Scott GK, Chu D, Kaur R, Malato J, Roshschild DE, Frazier K, Eppenberger-Castori S, Hann B, Park BH, Benz CC. ERpS294 is a biomarker of ligand or mutational ERα activation and a breast cancer target for CDK2 inhibition. Oncotarget 2016; 8: 83432–83445. [PubMed: 29137354]

33. Zhou Y, Zou H, Yau C, Zhao L, Hall SC, Drummond DC, Farr-Jones S, Park JW, Benz CC, Marks JD. Discovery of internalizing antibodies to basal breast cancer cells. Protein Eng Des Sel 2018; 31: 17–28. [PubMed: 29301020]

34. Neve RM, Chin K, Fridlyand J, Yeh J, Baehner FL, Fevr T, et al. A collection of breast cancer cell lines for the study of functionally distinct cancer subtypes. Cancer Cell 2006; 10: 515–27. [PubMed: 17157791]

35. Cancer Genome Atlas Research Network. Comprehensive molecular portraits of human breast tumours. Nature 2012; 490: 61–70. [PubMed: 23000897]

36. Hoadley KA, Yau C, Wolf DM, Cherniack AD, Tamborero D, Ng S, et al. Multiplatform analysis of 12 cancer types reveals molecular classification within and across tissues of origin. Cell 2014; 158: 1–16.

37. Srivastava D, Zhu W, Johnson WH Jr, Whitman CP, Becker DF, Tanner JJ. The structure of the proline utilization A proline dehydrogenase domain inactivated by *N*-propargylglycine provides insight into conformational changes induced by substrate binding and flavin reduction. Biochemistry 2010; 49: 560–569. [PubMed: 19994913]

38. Binda C, Hubalek F, Li M, Herzig Y, Sterling J, Edmondson DE, Mattevi A. Binding of rasagiline-related inhibitors to human monoamine oxidases: a kinetic and crystallographic analysis. J Med Chem 2005; 48: 8148–8154. [PubMed: 16366596]

39. Siegelin MD, Dohi T, Raskett CM, Orlowski GM, Powers CM, Gilbert CA, Ross AH, Plescia J, Altieri DC. Exploiting the mitochondrial unfolded protein response for cancer therapy in mice and human cells. J Clin Invest 2011; 121: 1349–1360. [PubMed: 21364280]

40. Münch C The different axes of the mammalian mitochondrial unfolded protein response. BMC Biology 2018; 16: 81. [PubMed: 30049264]

41. Jensen MB, Jasper H. Mitochondrial proteostasis in the control of aging and longevity. Cell Metabolism 2014; 20: 214–225. [PubMed: 24930971]

42. Wiechmann K, Muller H, Konig S, Wielsch N, Svatos A, Jauch J, Werz O. Mitochondrial chaperonin HSP60 is the apoptosis-related target for myrtucommulone. Cell Chemical Biology 2017; 24: 614–623. [PubMed: 28457707]

43. Eiyama A, Okamoto K. PINK1/Parkin-mediated mitophagy in mammalian cells. Curr Opin Cell Biol 2015, 33: 95–101. [PubMed: 25697963]

44. Liu W, Le A, Hancock C, Lane A, Dang CV, Fan TW-M, Phang JM. Reprogramming of proline and glutamine metabolism contributes to the proliferative and metabolic responses regulated by oncogenic transcription factor c-MYC. Proc Natl Acad Sci USA 2012; 109: 8983–8988. [PubMed: 22615405]

45. Wiley CD, Schaum N, Alimirah F, Lopez-Dominguez JA, Orjalo AV, Scott G, Desprez PY, Benz C, Davalos AR, Campisi J. Small-molecule MDM2 antagonists attenuate the senescence-associated secretory phenotype. Sci Rep 2018; 8: 2410. [PubMed: 29402901]

46. Shangary S, Qin D, McEachern D, Liu M, Miller RS, Qiu S, et al. Temporal activation of p53 by a specific MDM2 inhibitor is selectively toxic to tumors and leads to complete tumor growth inhibition. Proc Natl Acad Sci USA 2008; 105: 3933–3938. [PubMed: 18316739]

47. Tallarita E, Pollegioni L, Servi S, Molla G. Expression in Escherichia coli of the catalytic domain of human proline oxidase. Protein Expression Purif 2012; 82: 345–351.

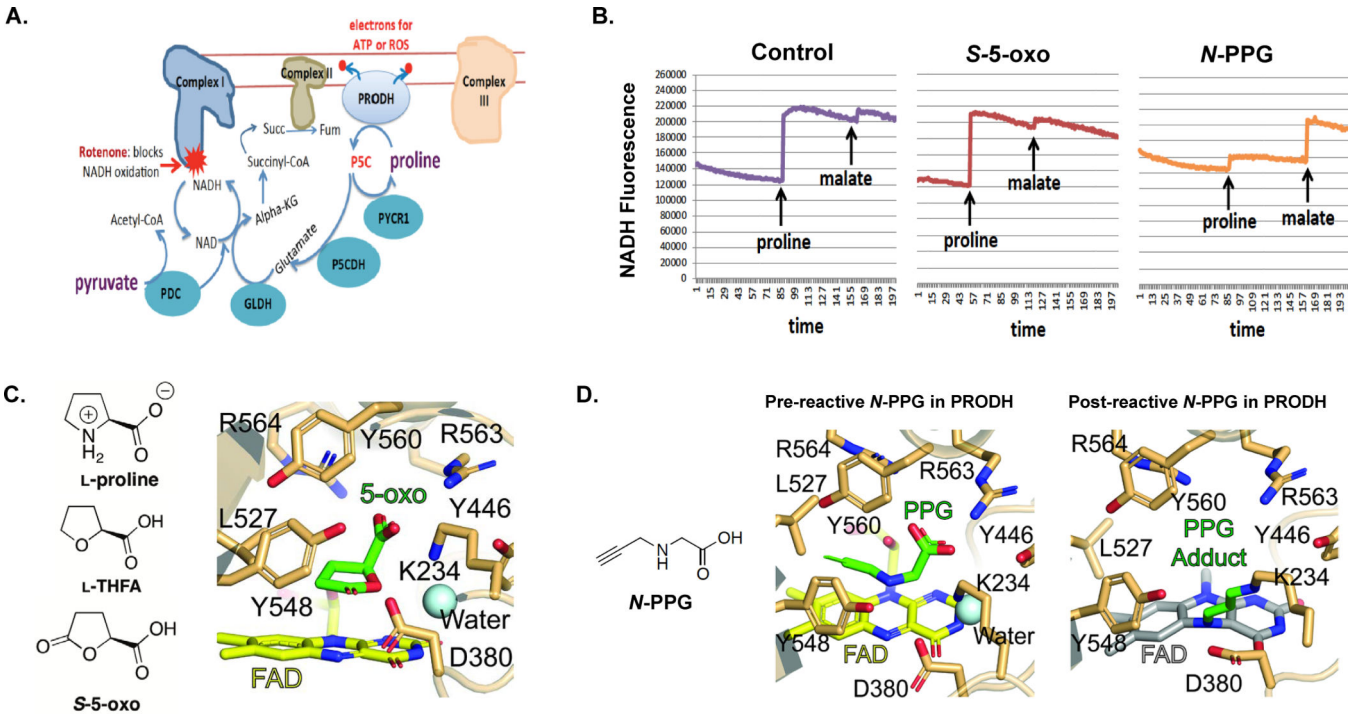

1.

Mitochondrial proline dehydrogenase (PRODH) and the effects of either reversible or irreversible substrate inhibitors. **A.** Mitochondrial PRODH catalyzes the first and rate-limiting step of proline oxidation to produce the unstable metabolic intermediate, P5C, with two electrons transferred into the electron transport chain for either ATP production or ROS generation (10–12). Also shown are the downstream mitochondrial reactions generating glutamate, α-ketoglutarate (KG), and NADH. Pyruvate oxidation by pyruvate decarboxylase (PDC) produces acetyl Co-A and increases the mitochondrial NADH pool, which is also increased by malate oxidation downstream of fumarase (fum). Rotenone blocks all Complex 1 oxidation of NADH to NAD, enabling fluorescence detection of mitochondrial NADH buildup as an assay for PRODH activity (11). **B.** Treating isolated ZR-75–1 mitochondria with either *S*-5-oxo or *N*-PPG inhibits proline oxidation (Supplement Figure 1). However, isolating and then washing (15 min) mitochondria from control, *S*-5-oxo or *N*-PPG pretreated (5 mM × 15 h) ZR-75–1 cell cultures and then assaying for NADH formation (fluorescence measurements every 8 sec for up to 30 min) in the presence of rotenone by sequential addition of proline (1 mM) followed by malate (1 mM) shows full restoration of PRODH activity to control levels in *S*-5-oxo treated cells but persistent inhibition of proline oxidation and NADH formation in *N*-PPG pretreated cells. **C.** Proline and two structural analogs (L-THFA, *S*-5-oxo), along with a computational model of the human PRODH catalytic pocket occupied by the co-substrate FAD, an intercalated water molecule, and the stereospecific PRODH competitive inhibitor, *S*-5-oxo, hydrogen bonded to the PRODH pocket tyrosine (Y548) and arginine (R564, R563) residues. **D.** *N*-propargylglycine (*N*-PPG) modelled inside the PRODH enzymatic pocket in both its pre-reactive (unbound) and post-reactive (bicovalently tethered to K234 and the N5 of FAD) states, the latter associated with pocket distortion as discussed in the text.

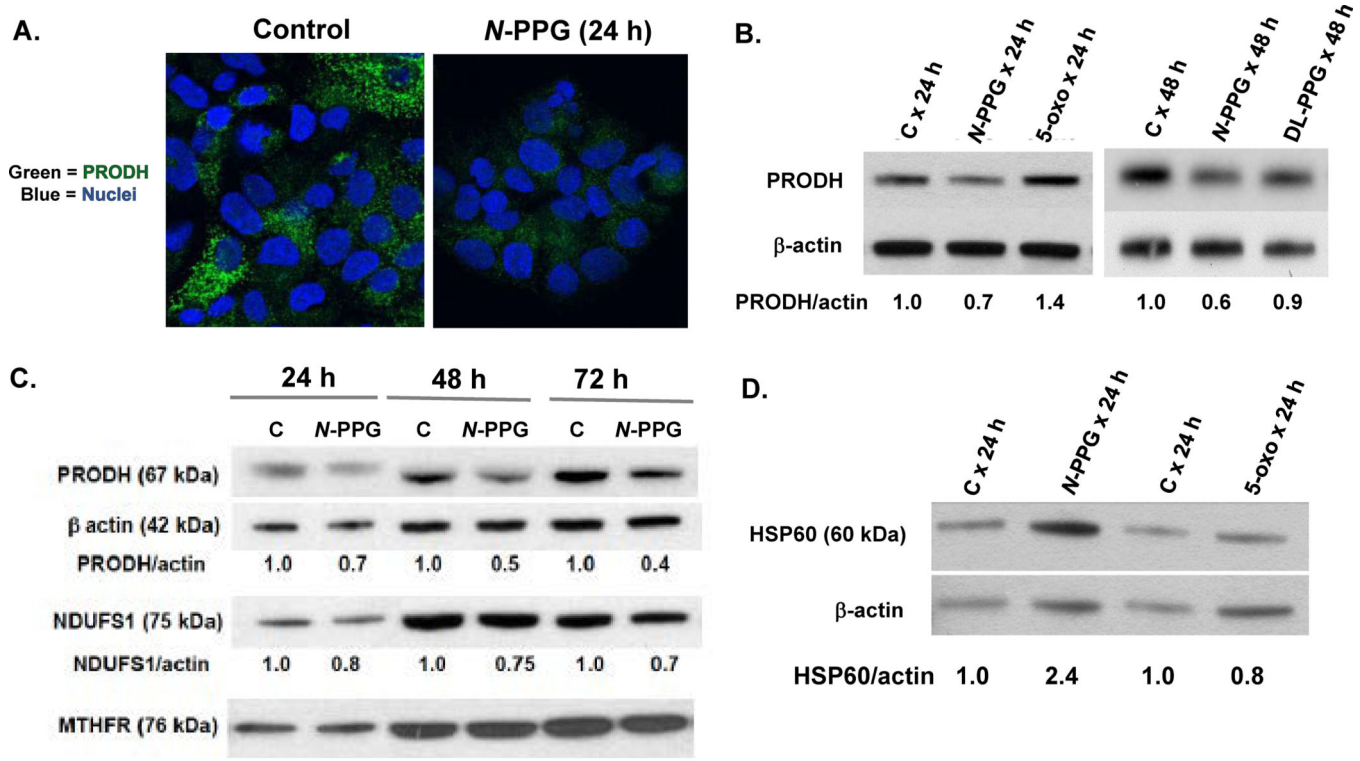

2.

Unlike competitive PRODH inhibitors, the suicide inhibitor *N*-PPG induces selective degradation of mitochondrial PRODH protein along with upregulation of the mitochondrial chaperone HSP60, consistent with UPR^{mt} induction. **A.** Confocal imaging of ZR-75–1 cells (63X oil immersion magnification) treated with vehicle (control) or *N*-PPG (5 mM × 24 h), nuclei stained with DAPI (blue) and PRODH stained with mouse primary and detected by a fluorochrome-conjugated secondary antibody (green). **B and C.** Western blotting shows 24–72 h degradation of PRODH (normalized to β-actin levels) by *N*-PPG but not by DL-PPG, and not seen affecting the mitochondrial NADH-ubiquinone oxidoreductase NDUFS1 or the cytosolic methylenetetrahydrofolate reductase MTHFR flavoprotein. While 5 mM *N*-PPG causes PRODH levels to begin degrading within 24 h, an equipotent dose of the PRODH competitive inhibitor *S*-5-oxo (5 mM) has no degrading effect on PRODH protein levels by 24–72 h. **D.** As PRODH levels degrade within 24 h of *N*-PPG (5 mM) exposure, levels of the mitochondrial chaperone HSP60 increase; *S*-5-oxo (5 mM) exposure produces no induction of mitochondrial HSP60.

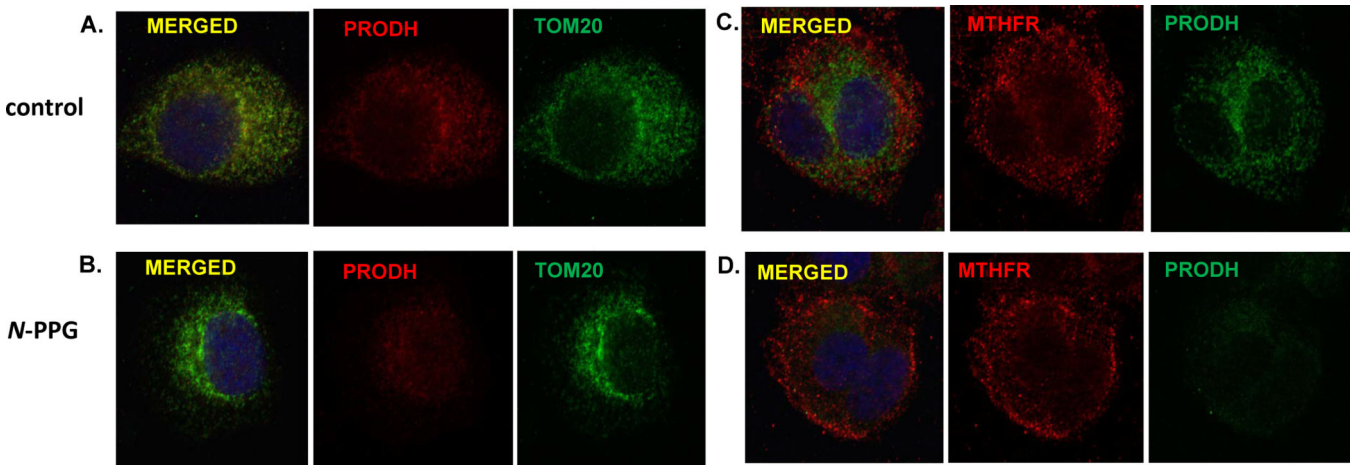

3.

Confocal imaging of control and *N*-PPG treated ZR-75–1 cell cultures shows early degradation in mitochondrial PRODH without loss of outer mitochondrial membrane component TOM20 or extramitochondrial FAD-containing enzyme MTHFR. **A.** Top left panel shows control (vehicle treated) ZR-75–1 cells stained for PRODH (red) and mitochondrial TOM20 (green), with merged images (yellow) confirming the mitochondrial localization of PRODH**. B.** Bottom left panel shows *N*-PPG treated (5 mM, 24 h) ZR-75–1 cells identically stained as in top left panel to reveal marked loss of mitochondrial PRODH. **C and D.** Top and bottom right panels show similar but independent experiment as in left panels except that control and *N*-PPG treated ZR-75–1 cells stained for PRODH used different primary (mouse monoclonal vs. rabbit polyclonal) and fluorochrome-conjugated secondary antibodies for comparison with the stained extramitochondrial flavoprotein MTHFR. Merged images confirm the different subcellular localizations of PRODH and MTHFR, and *N*-PPG induced loss of PRODH without loss of MTHFR. (63X oil immersion magnification)

A. Mouse kidneys (PTC1797):

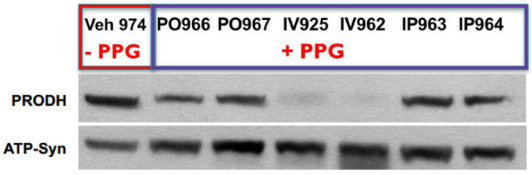

PRODH	21052	9954	13914	1958	274	16498	11511
ATP-Syn	7955	13377	19598	17504	18304	15352	13145
PRODH / ATP-Syn	2.65	0.74	0.71	0.11	0.01	1.07	0.88
% Control (-PPG)	100%	27.9%	26.8%	4.2%	0.4%	40.4%	33.2%

B. MCF7 xenografts (PTC1854):

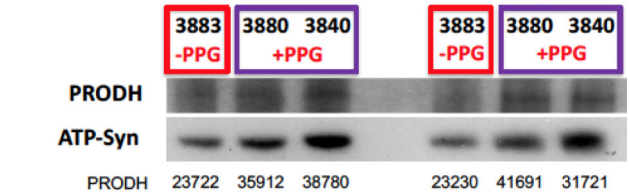

PRODH	23722	35912	38780	23230	41691	31721
ATP-Syn	4921	9485	14763	4588	9706	14140
PRODH / ATP-Syn	4.8	3.8	2.6	5.1	4.3	2.2
% Control (- PPG)	100%	79%	54%	100%	84%	43%

C. MCF7 xenografts (PTC1854):

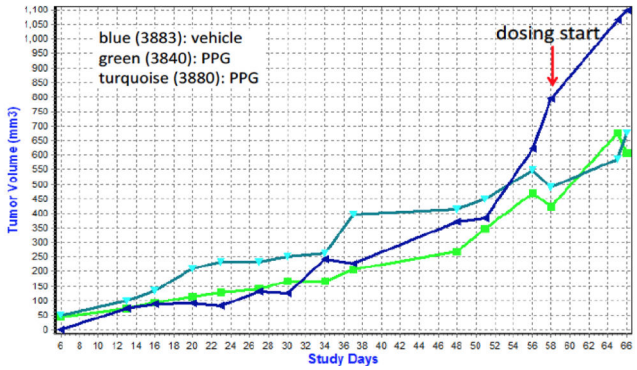

4.

PTC1797 and PTC1854 nude mouse xenograft studies comparing *in vivo N*-PPG treatment effects on resected mouse kidney and MCF7 xenograft PRODH protein expression. **A.** In PTC1797, control mice (including mouse 974) were given saline vehicle while the *N*-PPG treated mice (including 962, 963, 964, 966, 967) received three 50 mg/kg doses every other day by either oral (PO), intravenous (IV), or intraperitoneal (IP) injections, sacrificed within 3 h of the final treatment when their organs (including kidneys) were resected and snap frozen (liquid nitrogen), protein extracted and immunoblotted for PRODH and ATP synthase. **B.** In PTC1854 one xenografted mouse (3883) received nine daily oral saline doses while two others (3840, 3880) received nine daily oral doses of *N*-PPG (50 mg/kg) before sacrifice, tumor resection, mitochondria isolation, protein extraction and immunoblotting (technical replicates), as performed in PT1797. **C.** Vehicle and *N*-PPG treatment effects on MCF7 tumor volumes as recorded in PT1854.

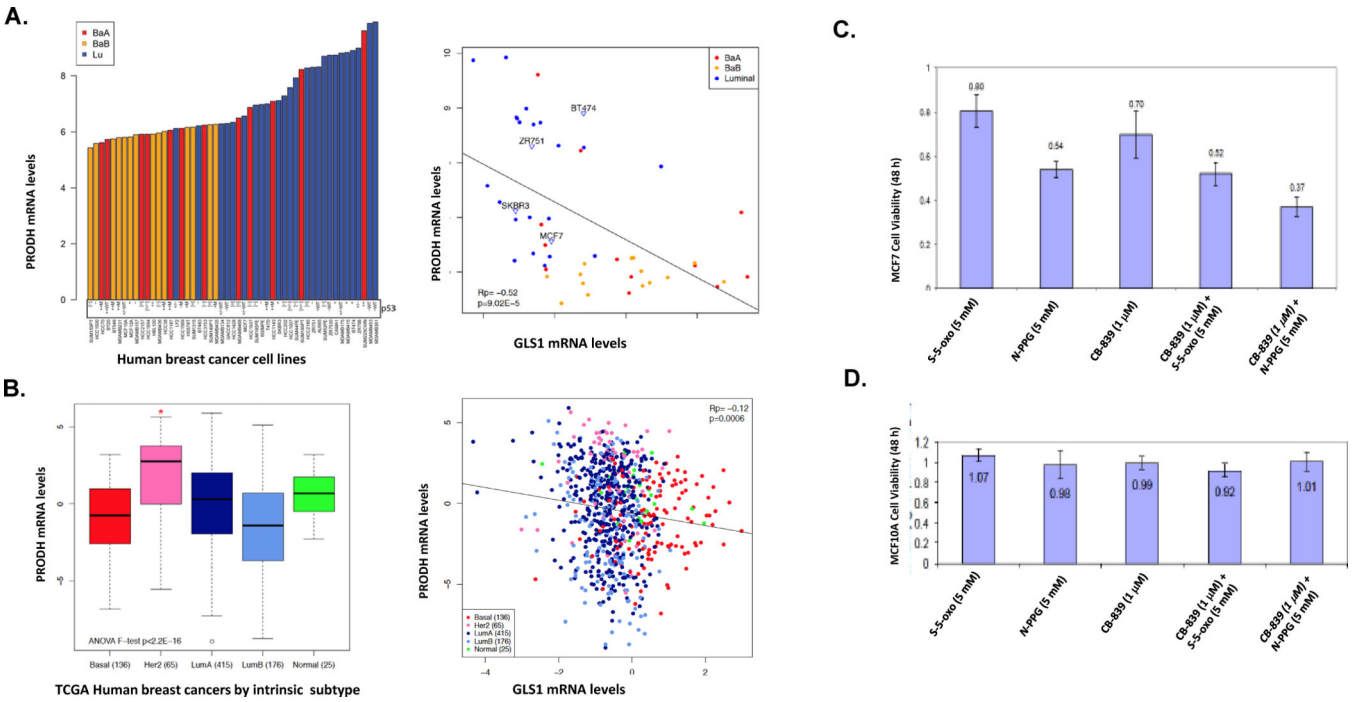

5.

In human breast cancer cell lines and primary tumors, PRODH and GLS1 expression are subtype dependent and anti-correlated, consistent with additive anti-cancer consequences observed when PRODH and GLS1 inhibitors are co-administered. **A.** PRODH mRNA expression levels (normalized, log2-scaled) across 51 different human breast cancer cell lines determined from published microarray data (34) and color-coded by breast cancer intrinsic subtype are highest in luminal (ER or PR+) and lowest in triple-negative breast cancer cells (left panel). Breast cancer cell line PRODH and GLS1 mRNA levels are significantly anti-correlated (right panel). **B.** Across 817 TCGA-collected and RNAseq analyzed primary human breast tumors (36), PRODH transcript levels also appear subtype dependent (left panel) and significantly anti-correlated with GLS1 transcript levels (right panel). **C.** As illustrated by MCF7 cancer cell line responses, combining the GLS1 inhibitor CB-839 with PRODH inhibitors, either *S*-5-oxo or *N*-PPG, produces additive reductions in cancer cell viability. **D.** As illustrated by the non-malignant epithelial cell line MCF10A, PRODH and GLS1 inhibitors given alone or in combination produce negligible effects on growth and viability.

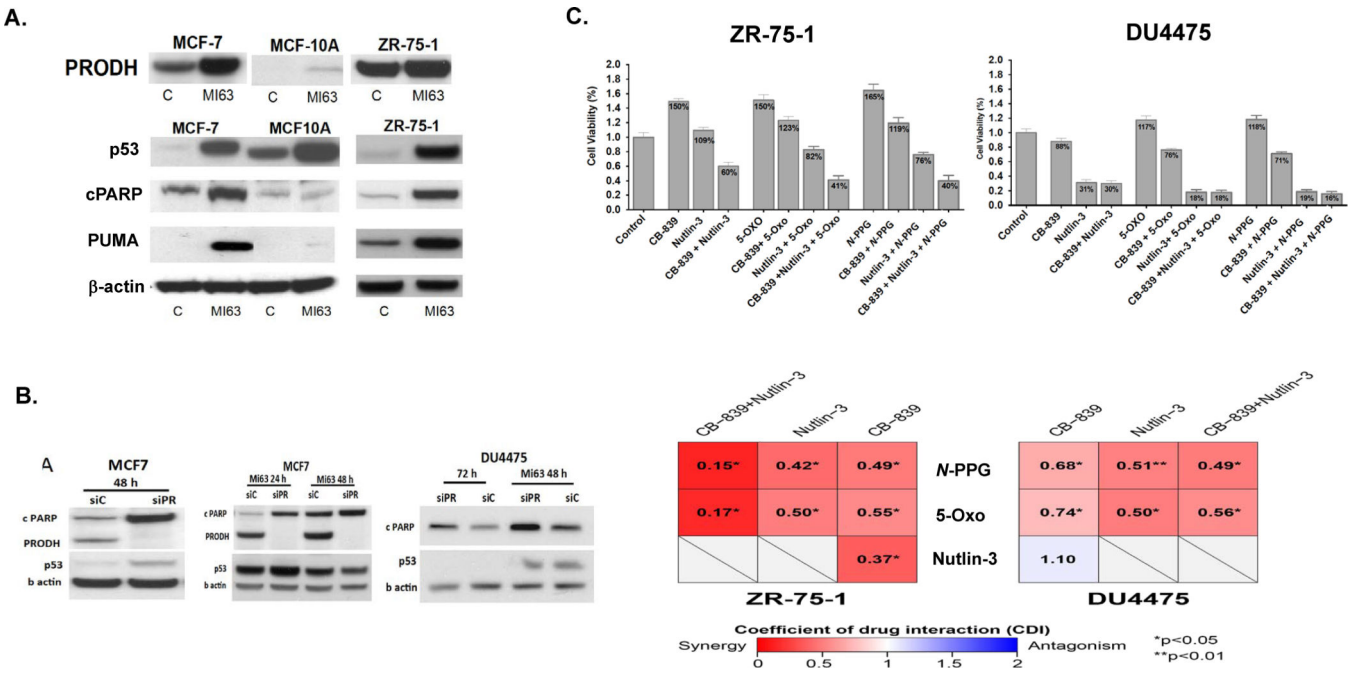

6.

While PRODH knockdown induces cancer cell apoptosis, the anti-cancer activity of PRODH inhibitors is enhanced by p53 upregulation and is optimally maximized in combination with both p53 upregulation and GLS1 inhibition. **A.** Upregulation of p53 in malignant (MCF7, ZR-75–1) and non-malignant (MCF10A) cells by the MDM2 inhibitor MI-63 (10 μM, 24 h) increases PRODH in all cells but induces apoptosis (cPARP and PUMA) only in malignant cells. **B.** PRODH knockdown by 48–72 h of siRNA treatment (vs. control siRNA) induces apoptosis (cPARP) in MCF7 and DU4475 cells that is further enhanced by 24–48 h of MI-63 co-treatment. **C.** ZR-75–1 and DU4475 cell viabilities (with error bars denoting SD) are synergistically and maximally reduced by combined PRODH inhibition (5 mM *S*-5-oxo or *N*-PPG × 72 h), GSL1 inhibition (5 μM CB-839 × 72 h) and p53 upregulation (5 μM Nutlin-3 × 72 h). The heat maps below bar graphs for each cell line (ZR-75–1, DU4475) reflect the calculated coefficient of drug interaction (CDI) score for each of the different drug combinations as indicated; red = synergy (CDI <1), blue = antagonism (CDI > 1), white = additivity (CDK =1), with significance indicated by * ($p < 0.05$) or ** ($P < 0.01$).